Density Functional Theory Study of Photophysical Properties of Iridium(III) Complexes with Phenylisoquinoline and Phenylpyridine Ligands

4 **AUTHORS**, INCLUDING:

Boris Minaev
Черкаський національний універси…
328 PUBLICATIONS **3,214** CITATIONS

SEE PROFILE

Hans Agren
KTH Royal Institute of Technology
867 PUBLICATIONS **18,824** CITATIONS

SEE PROFILE

Density Functional Theory Study of Photophysical Properties of Iridium(III) Complexes with Phenylisoquinoline and Phenylpyridine Ligands

Xin Li,[†,‡] Boris Minaev,[‡,§] Hans Ågren,*[,‡] and He Tian*[,†]

[†]Laboratory for Advanced Materials and Institute of Fine Chemicals, East China University of Science and Technology, Shanghai 200237, People's Republic of China

[‡]Department of Theoretical Chemistry, School of Biotechnology, Royal Institute of Technology, SE 10691 Stockholm, Sweden

[§]Bogdan Khmelnitskij National University, 18031 Cherkassy, Ukraine

ABSTRACT: Linear and quadratic response time-dependent density functional theory is applied to study the photophysical properties of iridium complexes with phenyliso-quinoline and phenylpyridine ligands. The ground-state geometries, frontier molecular orbitals, absorption spectra, phosphorescence wavelengths, and radiative rate constants are computed to facilitate better understanding of the structure–property relationships of these iridium complexes used in organic light-emitting diodes (OLEDs) to enhance spin–orbit coupling and triplet state emission. The agreement obtained between calculated and available experimental data indicates a possibility to guide the design of phosphorescence-based OLEDs by predicting their relevant properties through quantum mechanical calculations.
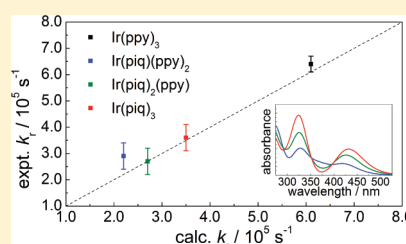
1. INTRODUCTION

Heavy transition-metal complexes with π-conjugated ligands are useful materials doped in organic light-emitting diodes (OLED) to make use of both singlet and triplet excitons and to provide better efficiency over commonly used organic conjugated polymers.[1−3] A typical structure of an electroluminescent device consists of a luminescent organic polymer film sandwiched between metal electrodes, from which electrons and holes are injected into polymers to form nearest-neighbor excitons. In pure organic polymers, the equal probability of the singlet and triplet colliding pairs[4] has limited the quantum yield of electroluminescence in OLEDs to within 25%,[5] whereas the remainder of the electric energy of the electron–hole recombination is consumed by triplet excitons just heating the polymer.

The presence of a heavy metal center significantly enhances the singlet–triplet transitions compared with typical organic π-conjugated polymer films like polyphenylene vinylene (PPV).[1] The spin-forbidden $T_1 \rightarrow S_0$ transition is activated by the spin–orbit coupling (SOC) effect, which is very weak in pure organic systems because of the negligible orbital angular momentum matrix elements between the singlet and triplet $\pi-\pi^*$ states[6,7] and the absence of heavy elements. It has been reported that the SOC-induced splitting of multiplets in the carbon atom is a thousand times smaller than that in iridium or platinum ions.[8,9] Baldo and coworkers have incorporated organometallic dyes containing heavy elements into the organic polymers to overcome spin-prohibition of the $T_1 \rightarrow S_0$ transition.[1−3] The prototype tris(2-phenylpyridine)iridium organometallic complex, or Ir(ppy)$_3$, with strong phosphorescence, has led to promising efficiency in

OLED devices,[1] and a large number of similar dyes have therefore been synthesized[5,10−14] to enhance the electroluminescence of OLEDs.[15,16] In such devices, the triplet states produced by electron–hole recombination also do useful work, providing 100% internal efficiency.

In particular, iridium(III) complexes with diverse organic π-conjugated ligands have shown strong phosphorescence in the visible region and have therefore attracted much attention in OLED fabrication.[14,16−21] The iridium ion is able to form efficient phosphorescent complexes with anionic 2-phenypyridine (ppy), 1-phenylisoquinoline (piq), acetylacetonate (acac), and 2-carboxy-4-aminopyridine and neutral bipyridine (bpy) ligands,[16−19,22−24] and more promisingly, the emission wavelength can be tuned from blue to red by introducing peripheral electron-donating or electron-with-drawing functional groups.[17,22−24]

Fundamental understanding of the structure–property relationship of the iridium complexes is of importance in the development of novel and better OLED devices. First-principle calculations have proven to give useful insight into electronic structure and photophysical properties of the prototype Ir(ppy)$_3$ complex.[25−27] In this Article, we present a density functional theory (DFT) study of the organometallic iridium(III) complexes with piq and ppy ligands, which have shown significance in OLED applications.[16] Time-dependent (TD) DFT using linear and quadratic response functions[28] allows us to establish connection
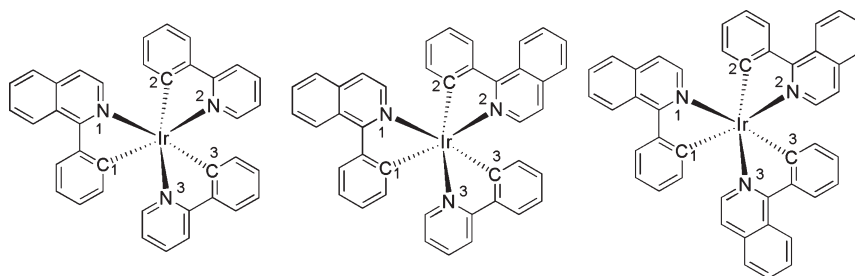
Figure 1. Chemical structures of the *fac*-Ir(piq)$_x$(ppy)$_{3-x}$ complexes (x = 1, 2, and 3 from left to right).

between the electronic structures and the photophysical properties and to investigate the energy transfer mechanism of the singlet—triplet transition, with the ultimate goal to interpret the origin of the high efficiency of OLED devices containing these complexes.

2. METHODS

The main contribution to the $S_0 \rightarrow T_1$ transition moment arises from the first-order corrected wave functions

$$M_j^i = \sum_{n=0}^{\infty} \frac{\langle S_0 | \hat{\mu}_j | S_n \rangle \langle S_n | \hat{H}_{SO} | T_1^i \rangle}{E(S_n) - E(T_1)}$$
$$+ \sum_{m=1}^{\infty} \frac{\langle S_0 | \hat{H}_{SO} | T_m \rangle \langle T_m | \hat{\mu}_j | T_1^i \rangle}{E(T_m) - E(S_0)}, \quad j \in \{x, y, z\} \quad (1)$$

where M_j^i is the j-axis projection ($j \in \{x,y,z\}$) of the electric dipole transition moment between the ground state and the ith spin sublevel of the triplet state and can be evaluated from the corresponding quadratic response function.[29] The triplet sublevels can be represented in terms of the spin eigenfunctions with spin projection on the z axis being a good quantum number in external magnetic field. In the zero field, the triplet spin sublevels are expressed by spin eigenfunctions with zero projections on three internal molecular axes, in which the zero-field splitting (ZFS) Hamiltonian is diagonalized.[8,15,29] The ZFS axes often coincide with molecular symmetry axes; from previous experience, we know that ZFS axes in Ir(III) complexes are close to directions determined by symmetry of the nearest metal-coordination sphere. Similar expectation is applicable in this study. Because only the averaged radiative rate constant (eq 3) is of interest in this study, any orthonormal set is applicable; the Cartesian components of the triplet state are here implemented.

The effective single-electron approximation[9,30] is used in the spin—orbit coupling operator $\hat{H}_{SO}$ in eq 1. This approximation removes the two-electron spin—orbit integrals and significantly reduces the computational cost. Previous experience has shown that the single-electron SOC operator together with the effective core potential (ECP) basis set can reproduce phosphorescence lifetimes within the error of 15%, comparing with the full relativistic four-component method.[31] Knowing M_j^i, the phosphorescence radiative rate constant from one of the three sublevels (indexed by i) of the lowest triplet state is[25]

$$k_r^i = k_r(S_0, T_1^i) = \frac{4\alpha_0^3}{3t_0} \Delta E_{S-T}^3 \sum_{j \in \{x, y, z\}} |M_j^i|^2 \quad (2)$$

where $t_0 = (4\pi\varepsilon_0)^2 \hbar^3 / m_e e^4$, α_0 is the fine-structure constant, and ΔE_{S-T} is the transition energy. At ambient temperature or in the

so-called high-temperature limit, the spin sublevel population was equalized by spin—lattice relaxation before the phosphorescent emission occurs, and the observed radiative rate constant k_r is equal to the algebraic average of the three k_r^i values

$$k_r = \frac{1}{3} \sum_{i=1}^{3} k_r^i \quad (3)$$

The ground-state geometries of the *fac*-Ir(piq)$_x$(ppy)$_{3-x}$ complexes were first optimized at the DFT level using the hybrid PBE0 exchange-correlation functional.[32] Several frequently used basis sets were tested to evaluate basis set dependence of the optimized geometry, including the Los Alamos ECP basis set (LANL2DZ),[33] Stuttgart/Dresden ECP basis set (SDD),[34] Dunning's valence/full double-ζ basis sets (D95 V and D95),[35] and Pople's 6-31G* basis set,[36] where the ECP basis sets are used only for the iridium atom. It turns out that the SDD ECP basis set for iridium together with the D95 basis set for lighter atoms performs better over the other combinations. The frontier molecular orbitals were then computed with the same functional and basis set and visualized by using the Gabedit software.[37] The singlet—singlet excitation energies were calculated by the TDDFT approach with the solvent effect of tetrahydrofuran (THF) taken into account by the conductor-like polarizable continuum model (C-PCM),[38,39] and the absorption spectrum was simulated through Gaussian convolution with a half-bandwidth of 0.2 eV. All computations above are carried out by using the Gaussian 09 program package.[40] Finally, the B3LYP functional[41] is used in the TDDFT linear and quadratic response calculations to compute phosphorescence wavelengths and radiative rate constants, as implemented in the Dalton code.[28,29]

3. RESULTS AND DISCUSSION

The chemical structures of the studied iridium complexes are shown in Figure 1. In the present work, we optimized the ground-state geometries of the *fac*-Ir(piq)$_x$(ppy)$_{3-x}$ complexes at the density functional level of theory, using the hybrid PBE0 functional which has been proven to predict reasonable structures of iridium complexes.[42,43] The basis set dependence of the computed iridium bond lengths in the *fac*-Ir(piq)$_2$(ppy) complex is listed in Table 1, together with the bond lengths from X-ray crystallography measurements.[16] The mean unsigned error (MUE) and mean signed error (MSE) between the computed and experimental bond lengths are computed to evaluate the basis set effect. It can be seen that the combination of LANL2DZ and 6-31G* gives the smallest MUE, whereas the MSE is still relatively large. Further inspection shows that the largest errors for LANL2DZ and 6-31G* occur for the Ir—N1 and Ir—N2 bond lengths. The combination of LANL2DZ and D95 V gives the smallest MSE

20725

dx.doi.org/10.1021/jp206279g |*J. Phys. Chem. C* 2011, 115, 20724–20731

Table 1. Basis Set Dependence of the Optimized Iridium Bond Lengths (in angstroms) for *fac*-Ir(piq)$_2$(ppy)

basis set (Ir, other)	Ir—N1	Ir—C1	Ir—N2	Ir—C2	Ir—N3	Ir—C3	MUE	MSE
LANL2DZ, D95 V	2.123	2.012	2.109	2.011	2.123	2.019	0.017	0.002
LANL2DZ, 6-31G*	2.158	2.005	2.142	2.004	2.155	2.010	0.015	0.015
SDD, D95	2.134	2.016	2.120	2.015	2.134	2.023	0.016	0.010
SDD, 6-31G*	2.161	2.013	2.145	2.011	2.157	2.017	0.020	0.020
exptl.[16]	2.126	1.996	2.124	1.985	2.149	2.003		

Table 2. Optimized Iridium Bond Lengths (in angstroms) for the *fac*-Ir(piq)$_x$(ppy)$_{3-x}$ Complexes (x = 0, 1, 2, and 3)

Compound	Ir—N1	Ir—C1	Ir—N2	Ir—C2	Ir—N3	Ir—C3
fac-Ir(ppy)$_3$	2.130	2.021	2.130	2.021	2.130	2.021
fac-Ir(piq)(ppy)$_2$	2.130	2.015	2.126	2.022	2.133	2.020
fac-Ir(piq)$_2$(ppy)	2.134	2.016	2.120	2.015	2.134	2.023
fac-Ir(piq)$_3$	2.129	2.017	2.123	2.014	2.134	2.016

but relatively large MUE. The mixed basis set of SDD and D95 is able to predict both Ir—N and Ir—C bonds with moderate errors. Considering both MUE and MSE, the combination of SDD and D95 performs better than the other tested combinations of basis sets and was therefore used exclusively in our subsequent calculations.

Table 2 presents the iridium bond lengths in the *fac*-Ir(piq)$_x$-(ppy)$_{3-x}$ optimized without symmetry restraints by using the PBE0 functional in combination with the mixed basis set of SDD and D95. The structure of the prototype *fac*-Ir(ppy)$_3$ was also calculated to provide insight into the effect of the piq ligands. It turned out that the optimized structure of *fac*-Ir(ppy)$_3$ was very close to pure C_3 symmetry. As x in *fac*-Ir(piq)$_x$(ppy)$_{3-x}$ increases, a clear influence is found in the Ir—C bond lengths. The Ir—C$_{ppy}$ bond lengths are in the range of 2.020 to 2.023 Å, and the Ir—C$_{piq}$ bond lengths become 2.014 to 2.017 Å. From *fac*-Ir(ppy)$_3$ to *fac*-Ir(piq)(ppy)$_2$, Ir—C1 and Ir—N2 are shortened while Ir—N3 is elongated. From *fac*-Ir(piq)(ppy)$_2$ to *fac*-Ir-(piq)$_2$(ppy), Ir—C2 and Ir—N2 are both shortened while Ir—C3 and Ir—N1 are elongated. From *fac*-Ir(piq)$_2$(ppy) to *fac*-Ir(piq)$_3$, Ir—C3 and Ir—N1 are shortened while Ir—N2 is elongated. In total, *fac*-Ir(piq)$_3$ has shorter Ir—C and Ir—N2 bonds, similar Ir—N1 bond, and longer Ir—N3 bond compared with *fac*-Ir(ppy)$_3$.

At the optimized ground-state structures, the calculated energy level diagram of the highest occupied molecular orbital (HOMO) and the lowest unoccupied molecular orbital (LUMO) in the *fac*-Ir(piq)$_x$(ppy)$_{3-x}$ complexes is shown in Figure 2. As x in *fac*-Ir(piq)$_x$(ppy)$_{3-x}$ increases from 0 to 3, the HOMO energy level is almost unchanged, while the LUMO is significantly lowered, in accordance with electrochemical data from experimental measurements.[16] Contour plots of the HOMO and LUMO are shown in Figure 3. In general, the HOMO consists of the d orbitals of iridium and the π orbitals of the ligands, which are mostly localized at the phenyl parts of the piq/ppy ligands, whereas the LUMO is delocalized on one or two of the piq ligands. In all complexes, the HOMO−LUMO transitions show mixed metal-to-ligand charge transfer (MLCT) and intraligand π−π* characteristics.

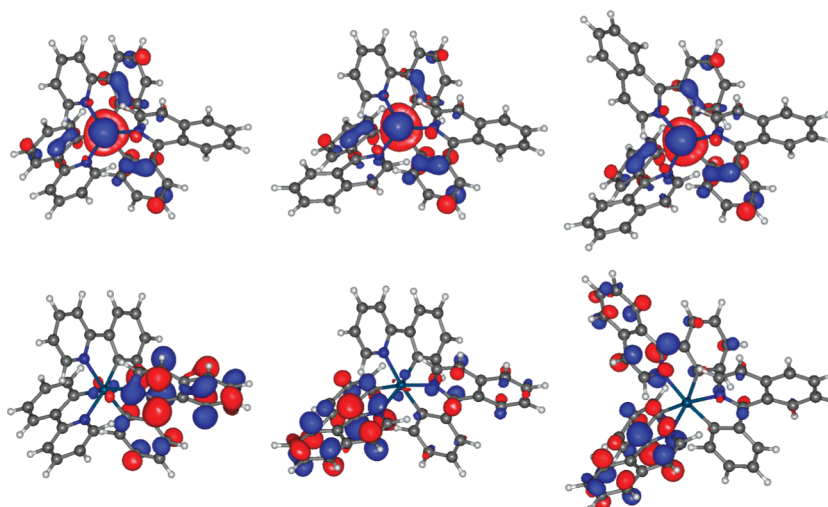The singlet−singlet excitation energies for the *fac*-Ir(piq)$_x$-(ppy)$_{3-x}$ complexes were calculated by TDDFT with the PBE0 functional and the mixed D95 and SDD basis set. The conductor-like polarizable continuum model[38,39] was used to simulate the
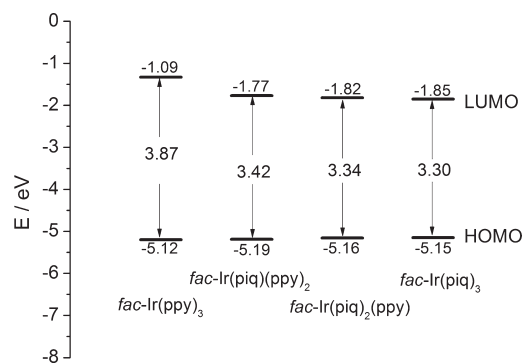
Figure 2. Calculated energy level diagram of HOMOs and LUMOs in the *fac*-Ir(piq)$_x$(ppy)$_{3-x}$ complexes (x = 0, 1, 2, and 3 from left to right).

solvent effect of THF, which is similar to 2-MeTHF used in the experiments.[16] The absorption spectrum was then simulated by using a Gaussian convolution with a half-bandwidth of 0.2 eV, as shown in Figure 4, where the absorption intensity is represented by the standard molar absorptivity in M^{-1} cm^{-1}. The stick spectra together with oscillator strengths are also shown in Figure 4, from which it is seen that a fraction of stick electronic bands is involved in the mixed MLCT and ligand-based π−π* transitions at wavelengths of 400−500 nm, whereas more bands are involved in the pure ligand-based π−π* transitions at wavelengths of 300−350 nm. The largest absorption wavelength in the stick spectrum is below 500 nm for singlet−singlet transitions, indicating that the weak absorption band at ~580 nm observed in experimental spectrum likely has triplet character, in accordance with the suggestion by Deaton et al.[16] Moreover, the positions of the absorption peaks are nicely reproduced compared with the experimental spectra.[16] The relative absorption intensity of these bands follows the order *fac*-Ir(piq)(ppy)$_2$ < *fac*-Ir(piq)$_2$(ppy) < *fac*-Ir(piq)$_3$, and the standard molar absorptivities are qualitatively reproduced. It should be noted that the computed molar absorptivities are dependent on the choice of the half-bandwidth, which is set to 0.2 eV in this work. Considering both the computed wavelengths and molar absorptivities, it is considered that our computational strategy is able to give satisfactory results.

It is interesting to see that the presence of the piq ligands results in a substantial enhancement of the absorption intensities in the MLCT bands. From the 400−500 nm region in the stick spectra, it is found that there are three dominant electronic transitions (with oscillator strength close to or larger than 0.1) for *fac*-Ir(piq)$_3$, two for *fac*-Ir(piq)$_2$(ppy), and one for *fac*-Ir(piq)(ppy)$_2$, leading to the increase in absorption intensity along with more piq ligands. In Tables 3 and 4, it can be seen that these transitions occur from HOMO−2 and HOMO−1, which contain large contribution from the Ir atom, to LUMO, LUMO+1, and LUMO+2, which mainly consist of contribution from the piq ligands. Therefore,

Figure 3. Calculated HOMOs (top) and LUMOs (bottom) of the *fac*-Ir(piq)$_x$(ppy)$_{3-x}$ complexes (*x* = 1, 2, and 3 from left to right).
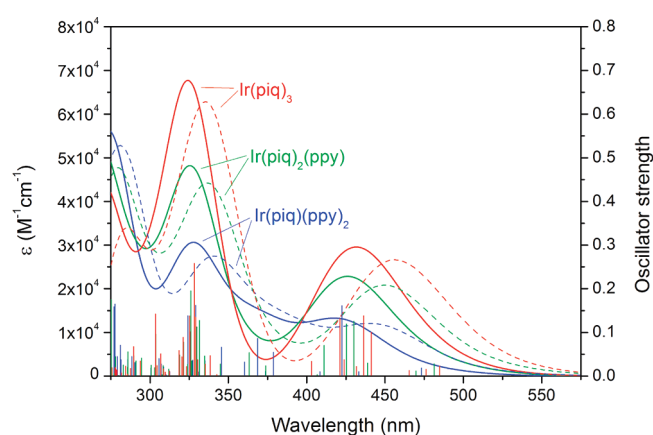
Figure 4. Calculated stick spectra of singlet−singlet excitation and simulated absorption spectra for the *fac*-Ir(piq)$_x$(ppy)$_{3-x}$ complexes (*x* = 1, 2, and 3). Full lines are obtained with the PBE0 functional, whereas dashed lines show the results from the B3LYP functional.

Table 3. Excitation Energies (*E*), Oscillator Strengths (*f*), and Composition in Terms of Molecular Orbital Contributions for the Dominant S$_0$ → S$_n$ Transitions at Wavelengths of 400−500 nm Calculated by PBE0 TDDFT Method

compound	state	*E* (eV, nm)	*f*	composition
fac-Ir(piq)$_3$	S$_4$	2.81, 441	0.0997	H−1 → L+0 (91%)
	S$_5$	2.84, 436	0.1380	H−2 → L+0 (93%)
	S$_8$	2.94, 421	0.1312	H−2 → L+1 (20%)
				H−1 → L+1 (15%)
				H−1 → L+2 (59%)
fac-Ir(piq)$_2$(ppy)	S$_4$	2.88, 430	0.1256	H−2 → L+0 (81%)
				H−1 → L+1 (11%)
	S$_5$	2.92, 425	0.1192	H−1 → L+1 (76%)
fac-Ir(piq)(ppy)$_2$	S$_3$	2.94, 422	0.1610	H−2 → L+0 (69%)
				H−1 → L+0 (26%)

the involvement of more piq ligands is expected to enhance the mixed MLCT and intraligand π−π* transitions and hence the

Table 4. Compositions of the Frontier Molecular Orbitals Involved in the Dominant S$_0$ → S$_n$ Transitions at Wavelengths of 400−500 nm, Calculated by PBE0 TDDFT Method

compound	MO	Ir (%)	1st ligand (%)	2nd ligand (%)	3rd ligand (%)
			piq	piq	piq
	L+2	5.6	19.6	44.1	30.7
	L+1	4.8	63.0	3.0	29.2
fac-Ir(piq)$_3$	L+0	2.0	13.2	49.2	35.6
	H−1	45.7	9.4	21.4	23.5
	H−2	52.4	21.6	12.4	13.6
			piq	piq	ppy
	L+1	5.2	61.4	31.7	1.7
	L+0	3.1	30.2	63.1	3.6
fac-Ir(piq)$_2$(ppy)	H−1	53.9	8.7	15.0	22.4
	H−2	50.6	21.7	19.0	8.7
			piq	ppy	ppy
	L+0	3.5	91.1	3.3	2.1
fac-Ir(piq)(ppy)$_2$	H−1	48.3	9.6	25.3	16.8
	H−2	52.1	24.4	9.9	13.6

absorption bands at wavelengths of 400−550 nm. There appear to be at least three overlapping bands in this region,[16] and our calculations also reproduce a set of electronic transitions with increasing intensity. (Only the most intense ones are shown in Table 3.) All of these bands are ligand-based π−π* transitions with strong admixture of MLCT character.

In Figure 4, we also included the absorption bands computed by the B3LYP functional as dashed lines. It can be seen that the results from the B3LYP functional suffer a red shift of ~25 nm, probably due to its less proportion of Hartree−Fock exchange than the PBE0 functional. It is clear that the PBE0 functional is superior to the B3LYP functional in computing both geometries and absorption bands of the Ir(III) complexes; nevertheless, the underestimation of singlet−singlet transition energy by the B3LYP functional is relatively small (~0.15 eV). It is also found that the B3LYP and PBE0 functionals give almost identical transitions among the frontier molecular orbitals upon

Table 5. Excitation Energies (E), Oscillator Strengths (f), Composition in Terms of Molecular Orbital Contributions and Spin−Orbit Coupling Matrix Elements for the Dominant $S_0 \rightarrow T_n$ Transitions at Wavelengths around 600 nm, Calculated by the B3LYP TDDFT Linear and Quadratic Response Method

compound	state	E (eV, nm)	f	composition	$\langle S_0|\hat{H}_{SO}|T_n \rangle$ (cm^{-1})
fac-Ir(piq)$_3$	T_1	1.99, 623	2.033×10^{-3}	H $- 0 \rightarrow$ L+0 (69%)	169
	T_2	2.04, 608	1.042×10^{-3}	H$-0 \rightarrow$ L+1 (63%)	506
	T_3	2.07, 599	1.668×10^{-3}	H$-0 \rightarrow$ L+2 (52%)	346
fac-Ir(piq)$_2$(ppy)	T_1	1.99, 622	1.536×10^{-3}	H$-0 \rightarrow$ L+0 (72%)	289
	T_2	2.06, 601	1.536×10^{-3}	H$-0 \rightarrow$ L+1 (65%)	397
fac-Ir(piq)(ppy)$_2$	T_1	2.05, 606	1.233×10^{-3}	H$-0 \rightarrow$ L+0 (71%)	391

Table 6. Phosphorescence Emission Wavelengths and Radiative Rate Constants Calculated at the Ground State Geometry Using B3LYP TDDFT Linear and Quadratic Response Theory In Comparison with Experimental Data

compound	$\lambda_{em,exptl}$/eV, nm	$\Delta E_{S-T,calcd}$/eV, nm	$k_{r,exptl}$/s^{-1}	$k_{r,calcd}$/s^{-1}
fac-Ir(ppy)$_3$	2.40, 517^a	2.48, 500	6.4×10^5^{a}	6.1×10^5
	2.39, 519^b			5.6×10^5^{b}
fac-Ir(piq)(ppy)$_2$	1.97, 631^c	2.05, 606	2.9×10^5^{c}	2.2×10^5
fac-Ir(piq)$_2$(ppy)	1.98, 627^c	1.99, 622	2.7×10^5^{c}	2.7×10^5
fac-Ir(piq)$_3$	1.99, 624^c	1.99, 623	3.6×10^5^{c}	3.5×10^5

^{a} In degassed CH$_2$Cl$_2$ at room temperature.[47] ^{b} In CH$_2$Cl$_2$ at ambient temperature.[48] ^{c} In 2-MeTHF at 293 K.[16]

singlet−singlet excitation (data not shown). In this regard, we choose to use the B3LYP functional to perform subsequent quadratic response calculations of the phosphorescence rate with SOC account, eqs 1−3, which is reasonable and is expected to give reliable results, as implied in previous papers.[44−46] We have also computed the $S_0 \rightarrow T_n$ transitions that are located in the low-energy region of the absorption spectra (wavelength longer than 580 nm), as shown in Table 5. The SOC matrix elements, which contribute to the first two terms in the sum, eq 1, for the $S_0 \rightarrow T_n$ transitions, are also given there. (Equation 1 can be easily generalized for the $S_0 \rightarrow T_n$ transition.) Account of $n = 0$ and $m = 1$ provides similar contributions, which together are proportional to the difference of the permanent dipole moments of the S_0 and T_1 states.[8] It can be seen that three transitions contribute the absorption spectra of fac-Ir(piq)$_3$, whereas only one transition contributes to that of fac-Ir(piq)(ppy)$_2$. This is in good agreement with the experimentally observed absorption intensity at ∼600 nm: fac-Ir(piq)$_3$ > fac-Ir(piq)$_2$(ppy) > fac-Ir(piq)(ppy)$_2$. Therefore it is concluded that the presence of piq ligands enhances both singlet−singlet and singlet−triplet absorption bands.

In the present work, we have employed the TDDFT quadratic response approach to compute the $S_0 \rightarrow T_n$ transition moment at the ground-state equilibrium structure, using the hybrid B3LYP functional (Table 5). Quadratic response theory offers some formal advantages in computing phosphorescence rates because it implements a complete summation over excited states in an operator gauge invariant manner.[28] In Table 6, we present the calculated singlet−triplet (S−T) transition energies together with the experimental values.[16,47,48] The S−T transition energies are computed by the linear response approach; previous experience has shown that ΔE_{S-T} coincides well with the highest phosphorescence peak.[44−46] From Table 6, it can be seen that the emission energies of fac-Ir(ppy)$_3$ and fac-Ir(piq)(ppy)$_2$ are slightly overestimated by the computed ΔE_{S-T}, the errors being

smaller than 0.1 eV. The experimental emission energies for fac-Ir(piq)$_2$(ppy) and fac-Ir(piq)$_3$ complexes are nicely reproduced by the calculated S−T transition energy. The computed vertical ΔE_{S-T} value serves as a good approximation to the phosphorescence emission energy.

Also listed in Table 6 are the theoretically calculated radiative rate constants, $k_{r,calcd}$, which correspond to the high-temperature limit of k_r. The numbers are to be compared with experimental radiative rate constants obtained from the lifetime and quantum yield: $k_{r,exptl} = \Phi_{em}/\tau_0$, where Φ_{em} is the photoluminescence quantum yield and τ_0 is the observed emission decay time. The k_r values are nicely reproduced for the fac-Ir(ppy)$_3$, fac-Ir(piq)$_2$-(ppy), and fac-Ir(piq)$_3$ species, indicating a promising use of density functional theory calculations in studies of iridium complexes. For the fac-Ir(piq)(ppy)$_2$ complex, the k_r is underestimated; however, the error is relatively small, and $k_{r,calcd}$ and $k_{r,exptl}$ are still of the same order of magnitude. Overall, the accuracy and reliability of the theoretical computations are quite satisfactory.

It is noteworthy that the geometry employed in the computations is a critical factor that affects the results. In this work, we have calculated the electronic parameters of the T−S transition moment in terms of perturbation theory under vertical transition conditions. All perturbing states are fixed at the S_0 geometry because the transition ends in the S_0 state and its vibrations determine the vibronic parameters of the emission. In our previous work,[46] we have demonstrated that the $T_1 \rightarrow T_n$ and $S_0 \rightarrow S_n$ states significantly contribute to S−T transition moment at the S_0 geometry, and these contributions will be destroyed at the T_1 geometry. In fact, our calculations at the T_1 geometry suggest that the electronic T−S transition moment decreases as the geometry of the molecule is changed from S_0 to T_1 and that the energy of the vertical $T_1 \rightarrow S_0$ transition is much smaller (data not shown), not only smaller than the 0−0 transition energy but even smaller than the expected maximum of the phosphorescence band. This is evident because at the T_1 geometry the ground singlet S_0 state energy is strongly lifted, making the T−S gap become artificially very low. The radiative rate constant is proportional to the cube of the energy gap and it is highly underestimated by direct quadratic response calculations at the T_1 geometry. Therefore, the computed lifetime τ would be unreasonably large at this excited T_1 state geometry. Besides, at room temperature (300 K) the phosphorescence band is wide and structureless; both 0−0 and other vibronic transitions contribute to the phosphorescence band. In this case, the vertical $S_0 \rightarrow T_1$ band corresponds to the most intense peak in both absorption and emission spectra and is used in our calculation to obtain the radiative rate constant k_r.

Of course, the $S_0 \rightarrow T_1$ absorption at 580 nm is shifted to higher energy than the $T_1 \rightarrow S_0$ emission (624 nm).[16] The large

20728

dx.doi.org/10.1021/jp206279g |*J. Phys. Chem. C* 2011, 115, 20724–20731

Stokes shift clearly indicates a relatively large geometry distortion at the triplet state equilibrium with respect to the ground S_0 state, which is in agreement with our geometry optimizations. Therefore, a good coincidence between the calculated and experimental phosphorescence wavelength is to some extent a result of error cancellation. In fact, our linear response calculations systematically underestimate the vertical $S_0 \rightarrow T_1$ transition energy. Despite some occasional agreement for the calculated and experimental phosphorescence wavelengths, we need to stress that the agreement for the radiative rate constants k_r is much more reliable. The electric dipole S−T transition moment, eq 1, is determined by summation of a huge amount of contributions by the quadratic response approach, which in fact implements the complete summation over states. The total scheme and pattern structure of these contributions for the S−T transition are more relevant when determined at the S_0 state geometry. This follows also from previous analysis of phosphorescence from $Ir(ppy)_3$ and other similar complexes.[25,27,44−46]

The structure−property relationship is indeed important in the design of promising OLED materials, and theoretical calculations are able to provide insight into this perspective. In our study, the singlet−triplet (S−T) transition energy is computed in vacuo by linear response theory, whereas the transition dipole moment is computed in vacuo by quadratic response theory. According to eq 2, the radiative rate constant k_r is proportional to the cube of the S−T transition energy and the square of the transition dipole moment. In this regard, the transition energy acts as an important factor that affects the magnitude of the radiative rate constant k_r. Our calculations show that the introduction of the first piq ligand into $Ir(ppy)_3$ leads to a 0.43 eV decrease in the transition energy (red shift of ~100 nm), in quantitative agreement with experimental observations.[16] Moreover, we noticed that the introduction of the first piq ligand significantly lower the energy level of the LUMO by 0.68 eV, which may lead to efficient interligand energy transfer (ILET), as suggested by Park et al.[23] The ILET is also evidenced by the fact that the LUMO is considerably localized on the piq ligand in the fac-$Ir(piq)(ppy)_2$ complex, as shown in Figure 3. Therefore, the involvement of ILET is one of the dominant factors that leads to the big difference between the radiative rate constant k_r of fac-$Ir(ppy)_3$ and fac-$Ir(piq)(ppy)_2$. This also provides an interpretation of the fact that the LUMO of fac-$Ir(piq)_3$ is not uniformly distributed among the three piq ligands but rather localized on two piq ligands.

As x increases from 1 to 3 in fac-$Ir(piq)_x(ppy)_{3−x}$, both singlet−singlet MLCT and ligand-based $\pi−\pi^*$ transitions at 300−500 nm are enhanced, indicating that the presence of more piq ligands is able to increase the $S_0 \rightarrow S_n$ transition dipole moment. Our previous Article suggests that in facial iridium complexes the $S_0 \rightarrow T_1$ transition intensity mainly arises from the $T_1 \rightarrow T_n$ and $S_0 \rightarrow S_n$ transitions,[46] and this could be one of the reasons for the increasing transition dipole moment and hence the radiative rate constant k_r. The spin−orbit coupling matrix element $\langle S_0|\hat{H}_{SO}|T_n\rangle$ is decreased for T_1 (Table 5); however, for T_2 and T_3, the fac-$Ir(piq)_3$ complex has much larger $\langle S_0|\hat{H}_{SO}|T_n\rangle$ values and similar transition energies, suggesting that there is probably a positive contribution to k_r, as indicated by the second summation notation in eq 1. With more piq ligands, the piq ligands contribute more to the LUMO (Table 4), and the IECT will be more efficient; both terms in eq 1 are enhanced, leading to considerable increase in the k_r value. This is in agreement with the experimental observation that the singlet−triplet bands

at ~600 nm are enhanced because of the piq ligands, suggesting that the $S_0 \rightarrow T_n$ transition dipole moment is increased. The result is that the introduction of the first piq ligand significantly lowers the radiative rate constant, whereas the second and the third piq ligands compensate this effect. The increasing k_r in fac-$Ir(piq)_x(ppy)_{3−x}$ complexes ($x = 1, 2,$ and 3) is also in accordance with the enhanced external quantum efficiency observed in experiments.[16]

Finally it is of use to look at the nonradiative rate constant k_{nr}. First, it can be seen from Figure 3 that the iridium d-orbital contribution to the LUMO becomes smaller as x increases from 1 to 3 in fac-$Ir(piq)_x(ppy)_{1−x}$, suggesting that the SOC matrix element between the ground singlet (S_0) and first excited triplet (T_1) states ($\langle S_0|\hat{H}_{SO}|T_n\rangle$) is becoming smaller. This complies with the fact that the HOMO−LUMO single-electron SOC integral is reduced when the involvement of iridium d orbital is negligible. Second, by performing DFT calculations with the use of linear response method, the SOC matrix element between the S_0 and T_1 states can be determined, as listed in Table 5. As x increases from 1 to 3, the value of $\langle S_0|\hat{H}_{SO}|T_1\rangle$ decreases from 391 to 169 cm^{-1}. Considering the fact that the square of the SOC matrix element determines the nonradiative quenching rate of the T_1 state to the ground S_0 state, a smaller value of the $\langle S_0|\hat{H}_{SO}|T_1\rangle$ integral will lead to lower intramolecular quenching rate of the T_1 state and higher quantum yield of phosphorescence. The experimentally measured k_{nr} is obtained as $k_{nr,expt} = (1 − \Phi_{em})/\tau_0$, being 4.3, 4.5, and 4.4 (in 10^5 s^{-1}) for fac-$Ir(piq)(ppy)_2$, fac-$Ir(piq)_2(ppy)$, and fac-$Ir(ppy)_3$, respectively. The computed SOC matrix element is not in qualitative agreement with experimental data, suggesting that the nonradiative decay path is probably related to the vibration of the complex and interaction with the environment; for a larger molecule, the probability of nonradiative decay due to vibrations or collisions would be larger, providing a possible interpretation for the nonmonotonic k_{nr} with respect to x.

4. CONCLUSIONS

We have presented DFT linear and quadratic response calculations of photophysical properties of the fac-$Ir(piq)_x(ppy)_{3−x}$ complexes ($x = 0, 1, 2,$ and 3) with phenylisoquinoline and phenylpyridine ligands. The ground-state Ir−N and Ir−C bond lengths were compared with the crystal structure of fac-$Ir(piq)_2$-(ppy). Good agreement has been achieved at the employed density functional level of theory. The HOMOs of these complexes were found to be mainly localized on the metal center and the phenyl ring of the piq/ppy ligands, whereas the LUMOs are delocalized on one or two of the piq ligands. The absorption spectra were simulated by Gaussian convolutions of the TDDFT calculated line positions; both of the MLCT bands and the absorption intensities were well-reproduced. It was concluded that the vertical $S_0 \rightarrow T_1$ transition has a mixed intraligand $\pi−\pi^*$ and MLCT character. Quadratic response computations at the ground-state geometries were found to give promising and satisfactory results compared with experimental data; the phosphorescence radiative rate constants were predicted with considerable accuracy. The computations suggest that the increase in x from 1 to 3 in the fac-$Ir(piq)_x(ppy)_{3−x}$ complexes can lead to a slightly narrowed HOMO−LUMO gap, enhanced absorption intensity, and an increased radiative rate constant k_r, in accordance with experimental observations. The presence of more piq

20729

dx.doi.org/10.1021/jp206279g |*J. Phys. Chem. C* 2011, 115, 20724−20731

ligands is expected to enlarge the S–T transition dipole moments, facilitating better efficiency in OLED devices.

The choice of the S_0 geometry in phosphorescence rate calculations can seem rather questionable at first glance, but the calculation practice[6–8] definitely supports this choice, especially in the case of heavy elements.[4,25,29,44–46,49] The most important perturbation patterns develop at this geometry. Because a complete theoretical solution of the S–T transition moment problem in a large molecule upon integration on all vibronic parameters is impossible now, one has to follow the practical semiempirical recommendation proposed above being based on the S_0 geometry calculation of eq 1. With this work, we show that DFT calculations with the effective single-electron spin–orbit approximation are powerful for studies of iridium complexes and can serve as important supplements to experiments in building structure–property relationships and guiding the synthesis of more efficient phosphorescence-based OLED dyes.

■ AUTHOR INFORMATION

Corresponding Author
*E-mail: agren@theochem.kth.se (H.Å.); tianhe@ecust.edu.cn (H.T.)

■ ACKNOWLEDGMENT

■ REFERENCES

(1) Baldo, M. A.; O'Brien, D. F.; You, Y.; Shoustikov, A.; Sibley, S.; Thompson, M. E.; Forrest, S. R. *Nature* **1998**, *395*, 151–154.

(2) Baldo, M. A.; Lamansky, S.; Burrows, P. E.; Thompson, M. E.; Forrest, S. R. *Appl. Phys. Lett.* **1999**, *75*, 4–6.

(3) Baldo, M. A.; Forrest, S. R. *Phys. Rev. B* **2000**, *62*, 10958–10966.

(4) Minaev, B.; Jansson, E.; Ågren, H.; Schrader, S. *J. Chem. Phys.* **2006**, *125*, 234704.

(5) Cao, Y.; Parker, I. D.; Yu, G.; Zhang, C.; Heeger, A. J. *Nature* **1999**, *397*, 414–417.

(6) Knuts, S.; Minaev, B. F.; Ågren, H.; Vahtras, O. *Theor. Chim. Acta.* **1994**, *87*, 343–371.

(7) Minaev, B. F.; Jonsson, D.; Norman, P.; Ågren, H. *Chem. Phys.* **1995**, *194*, 19–31.

(8) Ågren, H.; Vahtras, O.; Minaev, B. *Adv. Quantum Chem.* **1996**, *27*, 71–162.

(9) Koseki, S.; Fedorov, D. G.; Schmidt, M. W.; Gordon, M. S. *J. Phys. Chem. A* **2001**, *105*, 8262–8268.

(10) Wilson, J. S.; Dhoot, A. S.; Seeley, A. J. A. B.; Khan, M. S.; Köhler, A.; Friend, R. H. *Nature* **2001**, *413*, 828–831.

(11) Wohlgenannt, M.; Tandon, K.; Mazumdar, S.; Ramasesha, S.; Vardeny, Z. V. *Nature* **2001**, *409*, 494–497.

(12) Monkman, A. P.; Burrows, H. D.; Hamblett, I.; Navaratnam, S. *Chem. Phys. Lett.* **2001**, *340*, 467–472.

(13) Xu, D.; Xie, D.; Guo, H. *J. Chem. Phys.* **2002**, *116*, 10626–10635.

(14) Xu, M. L.; Zhou, R.; Wang, G. Y.; Xiao, Q.; Du, W. S.; Che, G. B. *Inorg. Chim. Acta* **2008**, *361*, 2407–2412.

(15) Finkenzeller, W. J.; Yersin, H. *Chem. Phys. Lett.* **2003**, *377*, 299–305.

(16) Deaton, J. C.; Young, R. H.; Lenhard, J. R.; Rajeswaran, M.; Huo, S. *Inorg. Chem.* **2010**, *49*, 9151–9161.

(17) Slinker, J.; Bernards, D.; Houston, P. L.; Abruña, H. D.; Bernhard, S.; Malliaras, G. G. *Chem. Commun.* **2003**, 2392–2399.

(18) De Angelis, F.; Fantacci, S.; Evans, N.; Klein, C.; Zakeeruddin, S. M.; Moser, J.-E.; Kalyanasundaram, K.; Bolink, H. J.; Gra1tzel, M.; Nazeeruddin, Md. K. *Inorg. Chem.* **2007**, *46*, 5989–6001.

(19) Bolink, H. J.; Coronado, E.; Santamaria, S. G.; Sessolo, M.; Evans, N.; Klein, C.; Baranoff, E.; Kalyanasundaram, K.; Graetzel, M.; Nazeeruddin, Md. K. *Chem. Commun.* **2007**, 3276–3278.

(20) Avilov, I.; Minoofar, P.; Cornil, J.; De Cola, L. *J. Am. Chem. Soc.* **2007**, *129*, 8247–8258.

(21) Di Censo, D.; Fantacci, S.; De Angelis, F.; Klein, C.; Evans, N.; Kalyanasundaram, K.; Bolink, H. J.; Grätzel, M.; Nazeeruddin, Md. K. *Inorg. Chem.* **2008**, *47*, 980–989.

(22) Lamansky, S.; Djurovich, P.; Murphy, D.; Abdel-Razzaq, F.; Kwong, R.; Tsyba, I.; Bortz, M.; Mui, B.; Bau, R.; Thompson, M. E. *Inorg. Chem.* **2001**, *40*, 1704–1711.

(23) You, Y.; Park, S. Y. *J. Am. Chem. Soc.* **2005**, *127*, 12438–12439.

(24) De Angelis, F.; Santoro, F.; Nazeruddin, Md. K.; Barone, V. *J. Phys. Chem. B* **2008**, *112*, 13181–13183.

(25) Jansson, E.; Minaev, B.; Schrader, S.; Ågren, H. *Chem. Phys.* **2007**, *333*, 157–167.

(26) Hay, P. J. *J. Phys. Chem. A* **2002**, *106*, 1634–1641.

(27) Nozaki, K. *J. Chin. Chem. Soc.* **2006**, *53*, 101–112.

(28) Vahtras, O.; Ågren, H.; Jørgensen, P.; Jensen, H. J. Aa.; Helgaker, T.; Olsen, J. *J. Chem. Phys.* **1992**, *97*, 9178–9187.

(29) Minaev, B.; Ågren, H. *Chem. Phys.* **2005**, *315*, 215–239.

(30) Koseki, S.; Schmidt, M. W.; Gordon, M. S. *J. Phys. Chem. A* **1998**, *102*, 10430–10435.

(31) Jansson, E.; Norman, P.; Minaev, B.; Ågren, H. *J. Chem. Phys.* **2006**, *124*, 114106.

(32) Perdew, J. P.; Burke, K.; Ernzerhof, M. *Phys. Rev. Lett.* **1996**, *77*, 3865–3868.

(33) Hay, P. J.; Wadt, W. R. *J. Chem. Phys.* **1985**, *82*, 270–283.

(34) Andrae, D.; Häußermann, U.; Dolg, M.; Stoll, H.; Preuß, H. *Theor. Chim. Acta* **1990**, *77*, 123–141.

(35) Dunning, Jr., T. H.; Hay, P. J. In *Modern Theoretical Chemistry*; Schaefer, H. F., III, Ed.; Plenum: New York, 1976.

(36) Hehre, W. J.; Ditchfield, R.; Pople, J. A. *J. Chem. Phys.* **1972**, *56*, 2257–2261.

(37) Allouche, A.-R. *J. Comput. Chem.* **2011**, *32*, 174–182.

(38) Barone, V.; Cossi, M. *J. Phys. Chem. A* **1998**, *102*, 1995–2001.

(39) Cossi, M.; Scalmani, G.; Rega, N.; Barone, V. *J. Comput. Chem.* **2003**, *24*, 669–681.

(40) Frisch, M. J.; Trucks, G. W.; Schlegel, H. B.; Scuseria, G. E.; Robb, M. A.; Cheeseman, J. R.; Montgomery, J. A., Jr.; Vreven, T.; Kudin, K. N.; Burant, J. C.; Millam, J. M.; Iyengar, S. S.; Tomasi, J.; Barone, V.; Mennucci, B.; Cossi, M.; Scalmani, G.; Rega, N.; Petersson, G. A.; Nakatsuji, H.; Hada, M.; Ehara, M.; Toyota, K.; Fukuda, R.; Hasegawa, J.; Ishida, M.; Nakajima, T.; Honda, Y.; Kitao, O.; Nakai, H.; Klene, M.; Li, X.; Knox, J. E.; Hratchian, H. P.; Cross, J. B.; Bakken, V.; Adamo, C.; Jaramillo, J.; Gomperts, R.; Stratmann, R. E.; Yazyev, O.; Austin, A. J.; Cammi, R.; Pomelli, C.; Ochterski, J. W.; Ayala, P. Y.; Morokuma, K.; Voth, G. A.; Salvador, P.; Dannenberg, J. J.; Zakrzewski, V. G.; Dapprich, S.; Daniels, A. D.; Strain, M. C.; Farkas, O.; Malick, D. K.; Rabuck, A. D.; Raghavachari, K.; Foresman, J. B.; Ortiz, J. V.; Cui, Q.; Baboul, A. G.; Clifford, S.; Cioslowski, J.; Stefanov, B. B.; Liu, G.; Liashenko, A.; Piskorz, P.; Komaromi, I.; Martin, R. L.; Fox, D. J.; Keith, T.; Al-Laham, M. A.; Peng, C. Y.; Nanayakkara, A.; Challacombe, M.; Gill, P. M. W.; Johnson, B.; Chen, W.; Wong, M. W.; Gonzalez, C.; Pople, J. A. *Gaussian 09*, revision A.2; Gaussian, Inc.: Wallingford, CT, 2009.

(41) Becke, A. D. *J. Chem. Phys.* **1993**, *98*, 5648–5652.

(42) Nie, D.; Liu, Z.; Bian, Z.; Huang, C. *THEOCHEM* **2008**, *861*, 97–102.

(43) Li, X.; Zhang, Q.; Tu, Y.; Ågren, H.; Tian, H. *Phys. Chem. Chem. Phys.* **2010**, *12*, 13730–13736.

(44) Minaev, B.; Ågren, H.; De Angelis, F. *Chem. Phys.* **2009**, *358*, 245–257.

(45) Minaev, B.; Minaeva, V.; Ågren, H. *J. Phys. Chem. A* **2009**, *113*, 726–735.

20730

dx.doi.org/10.1021/jp206279g |*J. Phys. Chem. C* 2011, 115, 20724–20731

(46) Li, X.; Minaev, B.; Ågren, H.; Tian, H. *Eur. J. Inorg. Chem.* **2011**, 2517–2524.

(47) Endo, A.; Suzuki, K.; Yoshihara, T.; Tobita, S.; Yahiro, M.; Adachi, C. *Chem. Phys. Lett.* **2008**, *460*, 155–157.

(48) Hofbeck, T.; Yersin, H. *Inorg. Chem.* **2010**, *49*, 9290–9299.

(49) Minaev, B.; Li, X.; Ning, Z.; Tian, H.; Ågren, H. In *Organic Light Emitting Diode - Material, Process and Devices*; Ko, S. H., Ed.; InTech: Rijeka, Croatia, 2011; pp 61−100.

20731

dx.doi.org/10.1021/jp206279g |*J. Phys. Chem. C* 2011, 115, 20724–20731